Curiosity at Gale Crater, Mars: Characterization and Analysis of the Rocknest Sand Shadow

D. F. Blake,[1]* R. V. Morris,[2] G. Kocurek,[3] S. M. Morrison,[4] R. T. Downs,[4] D. Bish,[5] D. W. Ming,[2] K. S. Edgett,[6] D. Rubin,[7]† W. Goetz,[8] M. B. Madsen,[9] R. Sullivan,[10] R. Gellert,[11] I. Campbell,[11] A. H. Treiman,[12] S. M. McLennan,[13] A. S. Yen,[14] J. Grotzinger,[15] D. T. Vaniman,[16] S. J. Chipera,[17] C. N. Achilles,[2] E. B. Rampe,[2] D. Sumner,[18] P.-Y. Meslin,[19] S. Maurice,[19] O. Forni,[19] O. Gasnault,[19] M. Fisk,[20] M. Schmidt,[21] P. Mahaffy,[22] L. A. Leshin,[23] D. Glavin,[22] A. Steele,[24] C. Freissinet,[22] R. Navarro-González,[25] R. A. Yingst,[16] L. C. Kah,[26] N. Bridges,[27] K. W. Lewis,[28] T. F. Bristow,[1] J. D. Farmer,[29] J. A. Crisp,[14] E. M. Stolper,[15] D. J. Des Marais,[1] P. Sarrazin,[30] MSL Science Team‡

The Rocknest aeolian deposit is similar to aeolian features analyzed by the Mars Exploration Rovers (MERs) Spirit and Opportunity. The fraction of sand <150 micrometers in size contains ~55% crystalline material consistent with a basaltic heritage and ~45% x-ray amorphous material. The amorphous component of Rocknest is iron-rich and silicon-poor and is the host of the volatiles (water, oxygen, sulfur dioxide, carbon dioxide, and chlorine) detected by the Sample Analysis at Mars instrument and of the fine-grained nanophase oxide component first described from basaltic soils analyzed by MERs. The similarity between soils and aeolian materials analyzed at Gusev Crater, Meridiani Planum, and Gale Crater implies locally sourced, globally similar basaltic materials or globally and regionally sourced basaltic components deposited locally at all three locations.

The Mars Science Laboratory (MSL) rover Curiosity began exploring the surface of Mars on 6 August 2012 (universal time coordinated); until 13 September 2012, it conducted an initial engineering checkout of its mobility system, arm, and science instruments. Curiosity spent sols 57 to 100 (*1*) at a location named Rocknest, collecting and processing five scoops of loose, unconsolidated materials extracted from an aeolian sand shadow (*2*).

Five scoops of material from the Rocknest sand shadow were individually collected and sieved (<150 μm) by the Sample Acquisition, Sample Processing and Handling–Collection and Handling for In situ Martian Rock Analysis (SA/SPaH-CHIMRA) instrument (*3*). Scoops 1 and 2 were processed by CHIMRA and discarded to reduce (by entrainment and dilution) any terrestrial organic contamination that may have remained after a thorough cleaning on Earth (*4*) and to coat and passivate the interior surfaces of the collection device with Mars dust. Portions (40 to 50 mg) of scoops 3 and 4 were delivered to the Chemistry and Mineralogy (CheMin) instrument (*5*) and the "observation tray," a 7.5-cm-diameter flat Ti-metal surface used for imaging and analyzing scooped and sieved material with Curiosity's arm and mast instruments. Portions of scoop 5 were delivered to both CheMin and the Sample Analysis at Mars (SAM) quadrupole mass spectrometer/gas chromatograph/tunable laser spectrometer suite of instruments (*6*).

We describe the physical sedimentology of Rocknest and suggest possible sources for the material making up the sand shadow. We use Alpha-Particle X-ray Spectrometer (APXS) and CheMin data to determine the amounts and chemistry of the crystalline and amorphous components of the sand shadow and compare these results with global soil measurements from the Mars Exploration Rovers (MERs) and to basaltic martian meteorites analyzed on Earth.

Results

Description and Interpretation of the Rocknest Sand Shadow

The Rocknest sand shadow (*7*) is an accumulation of wind-blown sediment deposited in the lower-velocity lee of an obstacle in the path of the wind. The orientation of the sand shadow indicates that the constructive winds were from the north. The surface is composed of dust-coated, predominantly rounded, very coarse (1- to 2-mm) sand grains (Fig. 1A). Trenches created during the scooping show that these larger grains form an armored surface ~2 to 3 mm in thickness (Fig. 1B). Beneath the armored surface, the bedform interior consists of finer-grained material whose size distribution extends through the resolution limit of Mars Hand Lens Imager (MAHLI) images (~30 μm per pixel under the conditions of the observation) (*8*). Because of CHIMRA's 150-μm sieve, the larger grains that armor the surface could not be analyzed by CheMin.

Coarse sand grains that fell from the crust into the scoop-troughs lost their dust coating and show diversity in color, luster, and shape. Among the grains are gray and red lithic fragments, clear/translucent crystal fragments, and spheroids with glassy luster (Fig. 1C). Some grains showed bright glints in the martian sunlight, suggesting specular reflections from mineral crystal faces or cleavage surfaces [similar features were observed by the optical microscope on board the Mars Phoenix Lander (*9*)]. MAHLI images of a sieved portion of material deposited on the observation tray (*3*) showed a variety of particle types from clear to colored to dark, angular to spherical, and dull to glassy-lustered (Fig. 1D).

During the scooping process, fragments of the armored surface were cohesive to the extent that "rafts" of surface crust were laterally compressed and displaced forward, and fragments of the crust fell into the scoop hole as cohesive units (Fig. 1B). The surface crust was also fractured and broken into rafts during scuffing by rover wheels (a process by which an excavation is made into the subsurface of unconsolidated regolith by rotating a single rover wheel). Material beneath the crust also had some cohesion, as shown by the oversteep walls of the scoop scars (much greater than the angle of repose and vertical in some cases).

The sand shadow has a discernible internal structure. On the headwall and flanks of each scoop trench, a lighter-tone layer is apparent ~1 cm beneath and parallel to the dune surface (Fig. 1B). The origin of the layering is not understood, and three hypotheses are viable. First,

[1]National Aeronautics and Space Administration (NASA) Ames Research Center, Moffett Field, CA 94035, USA. [2]NASA Johnson Space Center, Houston, TX 77058, USA. [3]Department of Geological Sciences, University of Texas, Austin, TX 78712, USA. [4]Department of Geology, University of Arizona, Tucson, AZ 85721, USA. [5]Department of Geological Sciences, Indiana University, Bloomington, IN 47405, USA. [6]Malin Space Science Systems, San Diego, CA 92191, USA. [7]U.S. Geological Survey, Santa Cruz, CA 95060, USA. [8]Max-Planck-Institut für Sonnensystemforschung, 37191 Katlenburg-Lindau, Germany. [9]Niels Bohr Institute, University of Copenhagen, 2100 Copenhagen, Denmark. [10]Center for Radiophysics and Space Research, Cornell University, Ithaca, NY 14850, USA. [11]University of Guelf, Guelph, Ontario, N1G2W1, Canada. [12]Lunar and Planetary Institute, Houston, TX 77058, USA. [13]State University of New York–Stony Brook, Stony Brook, NY 11790, USA. [14]Jet Propulsion Laboratory/California Institute of Technology, Pasadena, CA 91109, USA. [15]California Institute of Technology, Pasadena, CA 91125, USA. [16]Planetary Science Institute, Tucson, AZ 85719, USA. [17]Chesapeake Energy, Oklahoma City, OK 73102, USA. [18]University of California, Davis, CA 95616, USA. [19]Institut de Recherche en Astrophysique et Planétologie (IRAP), UPS-OMP-CNRS, 31028 Toulouse, France. [20]Oregon State University, Corvallis, OR 97331, USA. [21]Finnish Meteorological Institute, FI-00101 Helsinki, Finland. [22]NASA Goddard Space Flight Center, Greenbelt, MD 20771, USA. [23]Rensselaer Polytechnic Institute, Troy, NY 12180, USA. [24]Geophysical Laboratory, Carnegie Institution of Washington, Washington, DC 20015, USA. [25]University Nacional Autonóma de México, Ciudad Universitaria, 04510 México D.F. 04510, Mexico. [26]Department of Earth and Planetary Sciences, University of Tennessee, Knoxville, TN 37996, USA. [27]The Johns Hopkins University Applied Physics Laboratory, Laurel, MD 20723, USA. [28]Princeton University, Princeton, NJ 08544, USA. [29]Arizona State University, Phoenix, AZ 85004, USA. [30]SETI Institute, Mountain View, CA 94043, USA.

*Corresponding author. E-mail: david.blake@nasa.gov
†Present address: Department of Earth and Planetary Sciences, University of California, Santa Cruz, CA 95064, USA.
‡MSL Science Team authors and affiliations are listed in the supplementary materials.

the layering may represent changes in bulk composition or grain size that occurred during deposition. Second, the layering may be the result of changes in oxidation state or other chemical properties that occurred after deposition, in which case the conformable nature of the banding and the surface of the sand shadow reflect depth-dependent postdepositional chemical processes. Finally, the layering may represent zones richer or poorer in light-toned dust, reflecting times of lesser or greater sand accumulation relative to the air-fall dust.

The aeolian bedform at Rocknest is quite similar to coarse-grained ripples encountered at Gusev by the MER Spirit (*10*, *11*) and at Meridiani Planum by the MER Opportunity (*12*, *13*) in that a coarse-grained, indurated, dust-coated surface overlies an interior of markedly finer sediment. Coarse-grained ripples on Earth typically consist of a surface veneer of coarse grains and a finer-grained interior (*7*, *14*), and the martian bedforms have been considered analogous features (*13*, *15*). The spatial grain-size sorting within coarse-grained ripples is thought to arise because of the short grain excursion length of the coarse grains traveling in creep and the much longer excursion length of finer saltating grains (*16*). With ripple migration, coarse grains are recycled through the bedform and become concentrated on the ripple surface, where impacts from saltating grains tend to buoy the grains upward.

Although the dynamics of sand shadows differ from those of coarse-grained ripples, and sand shadows on Earth do not characteristically show a coarse-grained surface, similar dynamics may arise owing to the mix-load transport of grains in creep and saltation. Alternate interpretations are also possible. First, the coarse-grained surface could represent a lag formed as winds deflated finer grains. However, the paucity of coarse grains within the interior indicates that an unreasonable amount of deflation would have had to occur to produce the veneer. Second, the coarse-grained veneer could represent the terminal growth phase of the bedform. Because the size of a sand shadow is fixed by the upwind obstacle size (*17*), once the terminal size is approached, the lower wind speeds that characterize the wake and allow for deposition of finer sediment are replaced by wind speeds that approach the unmodified (primary) winds. At this point, there would be selective deposition of coarse grains traveling in creep, whereas finer saltating grains would bypass the bedform. Third, the sand shadow could have formed largely by the more readily transported fine saltation load, but as the area became depleted in finer grains, more of the residuum of

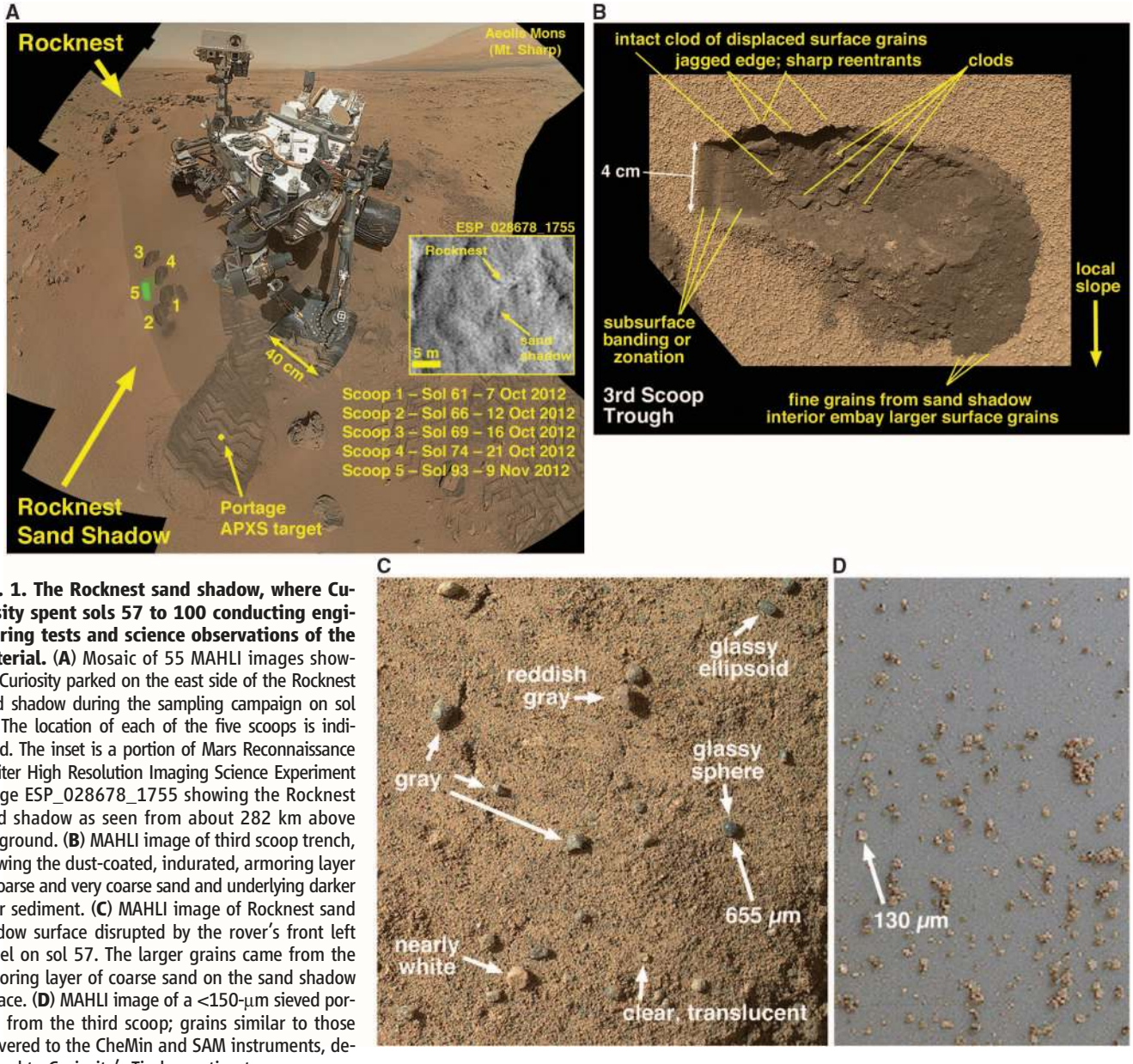

Fig. 1. The Rocknest sand shadow, where Curiosity spent sols 57 to 100 conducting engineering tests and science observations of the material. (**A**) Mosaic of 55 MAHLI images showing Curiosity parked on the east side of the Rocknest sand shadow during the sampling campaign on sol 84. The location of each of the five scoops is indicated. The inset is a portion of Mars Reconnaissance Orbiter High Resolution Imaging Science Experiment image ESP_028678_1755 showing the Rocknest sand shadow as seen from about 282 km above the ground. (**B**) MAHLI image of third scoop trench, showing the dust-coated, indurated, armoring layer of coarse and very coarse sand and underlying darker finer sediment. (**C**) MAHLI image of Rocknest sand shadow surface disrupted by the rover's front left wheel on sol 57. The larger grains came from the armoring layer of coarse sand on the sand shadow surface. (**D**) MAHLI image of a <150-μm sieved portion from the third scoop; grains similar to those delivered to the CheMin and SAM instruments, delivered to Curiosity's Ti observation tray.

coarser grains would be incorporated into transport, with the coarse-grained surface arising through subsequent deflation.

None of these interpretations explains the general absence of observed coarse grains in the interior; the contrast in grain size between the surface and the interior is more marked in the Rocknest sand shadow and in some of the coarse-grained ripples observed by MERs than in many Earth examples. This may reflect the greater impact energy of saltating grains on Mars compared with Earth and their ability to transport disproportionally larger grains in creep (*18*). Regarding the apparent absence of interior coarse grains, the small scooped areas may not be representative of the entire bedform, and interior horizons of coarse grains could easily have been bypassed. In addition, as seen with coarse-grained ripples on Earth, the amount of coarse sediment occurring in the interior varies and decreases with the supply of coarse grains.

Regardless of the origin of the coarse-grained surface, this armored surface would stabilize the bedform during all but the strongest wind events. In turn, the armored surface would allow time for surface induration to develop, further stabilizing the sand shadow. The similarity of the armoring and induration of the sand shadow at Rocknest to coarse-grained ripples encountered by Spirit and Opportunity suggests that the processes of grain transport and stabilization are similar across equatorial Mars and that Mars' winds (in recent eras) rarely were strong enough to transport sand grains of 1- to 3-mm diameter. To move the grains at the current atmospheric pressure of 0.02 kg/m^3, the wind velocities would need to be ~36 m/s (80 mph) and ~52 m/s (116 mph), with and without saltation, respectively. Under conditions of high obliquity, during which time the atmospheric pressure could increase to 0.04 kg/m^3, these values would decrease to 26 m/s (58 mph) and ~37 m/s (83 mph), respectively (see Materials and Methods). The potential antiquity of the Rocknest sand shadow is highlighted by comparing it with granule ripples on Meridiani Planum, where cratering postdates a field of pristine granule ripples and the crater count suggests an age of 50,000 to 200,000 years (*19*).

Mineralogy of the Rocknest Sand Shadow

Analysis and interpretation of the mineralogy of the Rocknest sand shadow is given in Bish *et al.* (*20*). Rocknest consists of both crystalline and x-ray amorphous components. The crystalline component is basaltic, composed of plagioclase feldspar, forsteritic olivine, and the pyroxenes augite and pigeonite (*20*). All of the minor phases are consistent with a basaltic heritage, with the exception of anhydrite and hematite. By constraining the compositions of the individual crystalline phases on the basis of their measured unit-cell parameters, the chemical compositions of the minerals of Rocknest were determined (*21*, *22*).

The crystalline component of Rocknest is chemically and mineralogically similar to that inferred for martian basalts across the planet and many of the basalts found in martian meteorites (Table 1) and, apart from somewhat lower Fe and K, broadly similar to estimates of the average martian crust (*23*). These basalts all contain (or have chemical compositions consistent with) the minerals olivine, augite, pigeonite, and plagioclase feldspar. The mineral proportions of the crystalline component of Rocknest are virtually identical to those calculated for the unaltered Adirondack class basalts from Gusev Crater (CIPW normative mineralogy from their APXS analyses) (Table 1) (*24*, *25*). Chemically, the mafic minerals of the Rocknest sediment (olivine, augite, and pigeonite) are all consistent with high-temperature chemical equilibria among Ca, Fe, and Mg at 1050 ± 75°C (Fig. 2). This consistency with chemical equilibria suggests, but does not prove, that these minerals and the plagioclase feldspar all derived from a common basaltic source rock, which was broken down into individual grains or lithic fragments and transported to Rocknest from regional source areas.

Bulk Chemistry of the Rocknest Sand Shadow

APXS provided an independent means of determining bulk chemistry of material in the Rocknest sand shadow. A measurement was made in a wheel scuff named Portage, which was largely devoid of surface crust (Fig. 1A). The chemical composition (taking into account analytical uncertainty) is within 2 SD of MER APXS analyses of basaltic soils (Table 2). The APXS chemistry of basaltic soils analyzed by the MERs at Gusev Crater and Meridiani Planum landing sites (Table 2) are within 1 SD of each other except for MgO and Na_2O, which are the same within 2 SD (*24*–*28*). The MER compositional averages exclude soils that contain a substantial local component (high SO_3 and high SiO_2 for Gusev and high Fe_2O_3 for Meridiani). The near identity of compositions of the Rocknest, Gusev, and Meridian basaltic soils implies either global-scale mixing of basaltic material or similar regional-scale basaltic source material or some combination thereof.

Table 1. Mineralogy of Rocknest soil [CheMin x-ray diffraction (XRD)] and normative mineralogies of basaltic materials from Gusev Crater and of martian meteorites. (Rocknest data are amorphous-free values.) Rocknest soil by CheMin (*20*), average of scoop 5, proportions of crystalline phases normalized to 100%; values in italics uncertain. CIPW norms (weight) for Gusev basaltic materials from MER APXS chemical analyses (*26*), ignoring S and Cl; Fe^{3+}/Fe_{tot} for Backstay and Irvine taken as 0.17, the value for an Adirondack basalt surface ground flat with the MER Rotary Abrasion Tool (RAT) (*26*). CIPW norms (wt %) of martian meteorites from bulk compositions; Fe^{3+}/Fe_{tot} as analyzed for Shergotty and Elephant Moraine (EETA) 79001A, estimated at 0.1 for Northwest Africa (NWA) 6234 and 0 for Queen Alexandra Range (QUE) 94201. K-spar is sanidine for the Rocknest soil, and normative orthoclase for others. Low-Ca Pyx is pigeonite for the soil and normative hypersthene for others. High-Ca Pyx is augite for the soil and normative diopside for others. Fe-Cr oxide includes magnetite, hematite, and chromite. All phosphorus in analyses are calculated as normative apatite. Mg no. is the % magnesium substituting for iron in the olivine structure, An refers to the % Ca substituting for Na in the plagioclase structure.

Location	Gale	Gusev			Meteorites			
Sample	Rocknest sand shadow	Adirondack	Backstay	Irvine	Shergotty	NWA 6234	EETA 79001A	QUE 94210
Quartz	*1.4*	0	0	0	0.2	0	0	3
Plagioclase	40.8	39	49	32	23	19	19	32
K-spar	*1.3*	1	6	6	1	0.5	0	0
Low-Ca Pyx	13.9	15	14	21	46	30	47	15
High-Ca Pyx	14.6	15	5	13	25	16	16	38
Olivine	22.4	20	15	16	0	27	13	0
Fe-Cr oxides	*3.2*	6	4	6	3	4	2	0
Ilmenite	*0.9*	1	2	2	2	2	1	4
Apatite	–	1	3	2	2	2	1	6
Anhydrite	*1.5*							
Mg no.	61 ± 3	57	62	55	51	63	63	40
An	57 ± 3	42	29	19	51	50	60	62

In contrast to the APXS measurement at the Portage wheel scuff, both CheMin and SAM measurements were carried out on the sieved, <150-μm-size fraction of soil. To discriminate potential differences between the fines delivered to CheMin and SAM and the bulk material analyzed in the wheel scuff, APXS chemistry was obtained from portions of sieved material deposited on the observation tray. APXS spectra from the bulk and sieved material are nearly identical, with the exception of a prominent Ti peak and increased background from the observation tray (reflecting Ti metal of the tray). Additionally, Ca, Mn, and Fe signals in spectra from the observation tray are lowered proportionally as a function of their atomic number, which suggests that a fraction of these grains is smaller than the APXS sampling depth (*29*). Slightly elevated S and Cl, with a S/Cl ratio similar to that found in soils by MERs (*30*), suggest a potential enrichment of these two elements in the <150-μm fraction delivered to the observation tray.

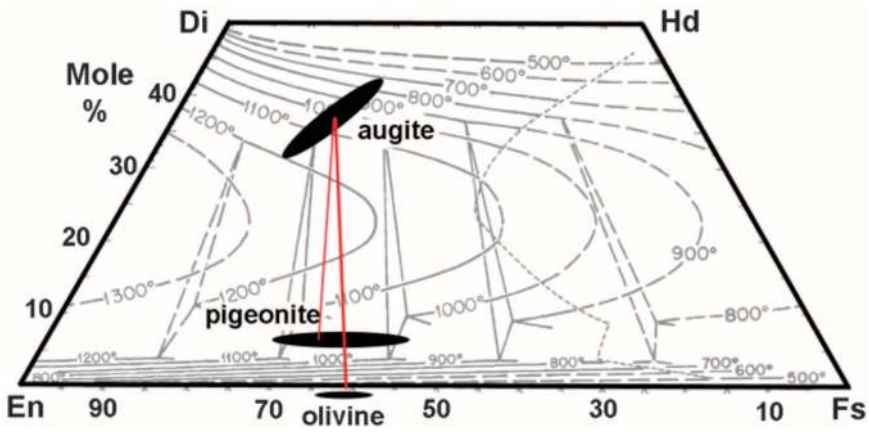

Fig. 2. Pyroxene compositional quadrilateral, showing the chemical and thermal relations between the major igneous minerals in the Rocknest sand shadow. Compositions of augite, pigeonite, and olivine in the Rocknest dune material, plotted on the pyroxene quadrilateral. En, enstatite, $Mg_2Si_2O_6$; Di, diopside, $CaMgSi_2O_6$; Hd, hedenbergite, $CaFeSi_2O_6$; and Fs, ferrosilite, $Fe_2Si_2O_6$. Pyroxenes are plotted within the quadrangle, based on CheMin XRD unit-cell parameters; olivine is plotted below the quadrilateral at the appropriate molar Mg/Fe ratio (*20*). Ellipses for each mineral approximate the uncertainties in mineral compositions from their unit-cell parameters. Gray background lines represent the surface of the pyroxene solvus, with temperatures in °C (*40*). Red lines are approximate equilibrium tie lines from the augite centroid composition to compositions of olivine and pigeonite, based on similar tie lines in an equilibrated anorthosite in lunar sample 62236 (*41*).

Table 2. Basaltic soil compositions from APXS analyses for Rocknest Portage, Gusev Crater, and Meridiani Planum.

	Rocknest	Gusev	Meridiani
Number	1*	48†	29†
SiO_2 (wt %)	42.88 ± 0.47	46.1 ± 0.9	45.7 ± 1.3
TiO_2	1.19 ± 0.03	0.88 ± 0.19	1.03 ± 0.12
Al_2O_3	9.43 ± 0.14	10.19 ± 0.69	9.25 ± 0.50
Cr_2O_3	0.49 ± 0.02	0.33 ± 0.07	0.41 ± 0.06
Fe_2O_3 + FeO	19.19 ± 0.12	16.3 ± 1.1	18.8 ± 1.2
MnO	0.41 ± 0.01	0.32 ± 0.03	0.37 ± 0.02
MgO	8.69 ± 0.14	8.67 ± 0.60	7.38 ± 0.29
CaO	7.28 ± 0.07	6.30 ± 0.29	6.93 ± 0.32
Na_2O	2.72 ± 0.10	3.01 ± 0.30	2.21 ± 0.18
K_2O	0.49 ± 0.01	0.44 ± 0.07	0.48 ± 0.05
P_2O_5	0.94 ± 0.03	0.91 ± 0.31	0.84 ± 0.06
SO_3	5.45 ± 0.10	5.78 ± 1.25	5.83 ± 1.04
Cl	0.69 ± 0.02	0.70 ± 0.16	0.65 ± 0.09
Br (μg/g)	26 ± 6	53 ± 46	100 ± 111
Ni	446 ± 29	476 ± 142	457 ± 97
Zn	337 ± 17	270 ± 90	309 ± 87
Sum (wt %)	99.85	99.88	99.88
Cl/SO_3	0.13 ± 0.02	0.12 ± 0.02	0.11 ± 0.01

*Gellert *et al.*, 2013 (*35*); analytical uncertainty. †±1SD of average.

To determine the amount and composition of the amorphous component, mass balance calculations were performed using the chemical composition of the bulk sample, the chemical compositions of the individual phases (e.g., plagioclase, sanidine, and olivine) and the relative proportions of those phases in the crystalline component. The empirical formulas of the major crystalline phases (Table 3) and their chemical compositions (table S2) were calculated from cell parameter data (*20*, *21*) (table S1). The chemical formulas and compositions of the minor crystalline components were assigned by stoichiometry (e.g., ilmenite as $TiFeO_3$). The relative proportions of amorphous and crystalline components and their respective bulk compositions are summarized in Table 4, with Rocknest having ~45 weight percent (wt %) amorphous and ~55 wt % crystalline components (*31*). The chemical compositions and proportions of amorphous and crystalline components were calculated on a light-element–free basis. The relative proportion of the amorphous component will in reality be greater than 45 wt % because the volatile inventory is associated with that component (*32*).

Abundance estimates for the x-ray amorphous component of a sample may vary considerably, depending on the method used for their determination. Bish *et al.* (*20*), for example, used a full pattern-fitting method together with known amorphous standard materials analyzed in the laboratory to determine the amount of amorphous or poorly crystalline material contained in the CheMin x-ray diffraction pattern. Their reported value of ~27 wt % ± 50% (1 SD range of 13 to 40 wt %), as calculated from diffraction and scattering data alone, is somewhat lower than the ~45% calculated from mass balance considerations, but both values are within the combined analytical uncertainty of the two techniques.

The inferred chemical composition of the amorphous component (Table 4) contains ~23% FeO + Fe_2O_3, suggesting that ferric nanophase oxide [npOx (*25*, *26*, *33*)] is present in abundance. Similarly, S (principally contained within the amorphous component) is closely associated with the npOx in dunes at the MER sites (*24*, *27*) as well. Abundances of SO_3 and Cl are correlated in soils from Gusev and Meridiani, which implies that both are associated with npOx in the amorphous component because these elements are not associated with Mg, Ca, or Fe in crystalline phases. The elements Cr, Mn, and P were associated with the amorphous component (Table 4), but

Table 3. Empirical chemical formulas of the four major phases identified in the Rocknest soil estimated by crystal-chemical techniques.

Phase	Formula
Olivine	$(Mg_{0.62(3)}Fe_{0.38})_2SiO_4$
Plagioclase	$(Ca_{0.57(13)}Na_{0.43})(Al_{1.57}Si_{2.43})O_8$
Augite	$(Ca_{0.75(4)}Mg_{0.88(10)}Fe_{0.37})Si_2O_6$
Pigeonite	$(Mg_{1.13(9)}Fe_{0.68(10)}Ca_{0.19})Si_2O_6$

they could instead be present as crystalline phases (e.g., Ca-phosphate and chromite) at abundances below the CheMin detection limit and/or as substitutional impurities in the major crystalline phases (e.g., Mn and Cr in pyroxene).

The SAM instrument analyzed Rocknest for volatile species and organic molecules (*32*), and it detected, in order of decreasing abundance, H_2O, SO_2, CO_2, and O_2. The crystalline phases, aside from a minor anhydrite component, do not include these species as a part of their structure, so they must either be present in the amorphous component or be present in the crystalline component at levels below the XRD detection limit, or both.

ChemCam spot observations in the scoop walls of Rocknest are characterized by the strong emissions from elemental hydrogen, although ChemCam is not sensitive to its bonding state (*34*). Comparison of this result with those of CheMin and SAM suggests that ChemCam detections of hydrogen most likely correspond to the H_2O associated with the amorphous component detected by CheMin.

Discussion

Global, Regional, and Local Sources

The crystalline phases in the Rocknest fines are consistent with a basaltic source and fit well within the measured qualitative mineralogy of basaltic martian meteorites and the normative mineralogy of Adirondack class olivine basalts at Gusev Crater (*25*) (Table 1). If the Rocknest assemblage of basaltic crystalline and amorphous components is locally derived, it is distinct from mafic float rocks analyzed to date by APXS and ChemCam in Gale Crater (*34*, *35*). This observation suggests that the similarity in the chemical compositions of aeolian bedforms (basaltic soil) at Gale, Gusev, and Meridiani (Table 2) might result from global-scale aeolian mixing of local-to-regional basaltic material that may or may not have variable chemical compositions. This process would require sufficiently strong winds occurring with sufficient frequency over a long enough time to achieve global or regional-scale transport of grains by saltation and suspension.

An alternative explanation for the comparable chemical compositions of aeolian bedforms at Gale, Gusev, and Meridiani is that the chemical compositions of martian basalts are similar at regional scales everywhere on the planet. The Rocknest sand shadow could reasonably have locally sourced 1- to 2-mm particles, with finer-grained regional basaltic material plus a contribution from global dust. The similarity of soil compositions (Table 2) suggests that the basaltic fine-grained materials at Gusev, Meridiani, and Gale Crater provide a reasonable approximation to the bulk composition of the exposed martian crust (*36*, *37*).

It is tempting to suggest that the light-toned martian dust is largely represented by the Rocknest amorphous component. However, we have no data to show that the <150-μm size fraction (clay to fine-sand size fraction) of material analyzed by CheMin has its finest material preferentially enriched in amorphous material. The evidence from MER for basaltic soils suggests that the chemical composition of the fine-grained, light-toned soil is approximately the same as the coarser-grained, dark-toned soils [e.g., table 10 in (*38*)].

The central mound of Gale Crater (Mt. Sharp or Aeolis Mons) exhibits reflectance spectra suggesting the presence of crystalline hydrated sulfate minerals and phyllosilicates (*39*), but neither was seen in Rocknest (above the 1 to 2% level). The absence of material from Mt. Sharp could arise from the wind pattern during formation of the Rocknest sand shadow; it is oriented so as to imply sediment transport from the north, and Mt. Sharp is east and southeast of Rocknest.

Materials and Methods

Calculation of Wind Speeds Required to Form the Rocknest Sand Shadow

The wind velocity required to move the coarse grains of the sand shadow by creep can be calculated. The critical shear velocity (u_{*c}) of the wind needed to transport 1-mm-diameter (d) grains is given by (*42*) as

$$u_{*_c} = \sqrt{0.0123\left(sgd + \frac{0.0003\ \mathrm{kg/s^2}}{\tilde{n}_f d}\right)}$$

where $s = \tilde{n}_s/\tilde{n}_f$, $\tilde{n}_s$ is the density of the grains using basalt (3000 kg/m^3), $\tilde{n}_f$ is the density of

Table 4. Chemical composition and proportion of XRD amorphous component in Rocknest Portage from APXS and CheMin data.

	Origin		Remove XRD crystalline component*										Composition	
	APXS†	APXS+ CheMin	Plagioclase	Sanidine	Olivine	Augite	Pigeonite	Ilmenite	Hematite	Magnetite	Anhydrite	Quartz	Amorphous‡	Crystalline
SiO_2, wt %	42.88	42.88	30.88	30.42	25.95	21.63	17.51	17.51	17.51	17.51	17.51	16.76	37.20	47.59
TiO_2	1.19	1.19	1.19	1.19	1.19	1.19	1.19	0.93	0.93	0.93	0.93	0.93	2.06	0.47
Al_2O_3	9.43	9.43	2.85	2.72	2.72	2.72	2.72	2.72	2.72	2.72	2.72	2.72	6.04	12.24
Cr_2O_3	0.49	0.49	0.49	0.49	0.49	0.49	0.49	0.49	0.49	0.49	0.49	0.49	1.09	0.00
FeO+Fe_2O_3§	19.19	10.43	10.43	10.43	10.43	10.43	10.43	10.43	10.43	10.43	10.43	10.43	23.14	-0.10
FeO-Cryst‖	—	7.37	7.37	7.37	3.31	2.29	0.59	0.35	0.35	0.00	0.00	0.00	-0.01	13.48
Fe_2O_3-Cryst¶	—	1.39	1.39	1.39	1.39	1.39	1.39	1.39	0.79	0.00	0.00	0.00	-0.01	2.55
MnO	0.41	0.41	0.41	0.41	0.41	0.41	0.41	0.41	0.41	0.41	0.41	0.41	0.91	0.00
MgO	8.69	8.69	8.69	8.69	4.97	3.72	2.19	2.19	2.19	2.19	2.19	2.19	4.86	11.86
CaO	7.28	7.28	4.65	4.65	4.65	3.19	2.87	2.87	2.87	2.87	2.53	2.53	5.61	8.67
Na_2O	2.72	2.72	1.62	1.60	1.60	1.60	1.60	1.60	1.60	1.60	1.60	1.60	3.56	2.03
K_2O	0.49	0.49	0.49	0.40	0.40	0.40	0.40	0.40	0.40	0.40	0.40	0.40	0.89	0.16
P_2O_5	0.94	0.94	0.94	0.94	0.94	0.94	0.94	0.94	0.94	0.94	0.94	0.94	2.09	-0.01
SO_3	5.45	4.96	4.96	4.96	4.96	4.96	4.96	4.96	4.96	4.96	4.96	4.96	11.01	-0.05
SO_3-Cryst#	—	0.49	0.49	0.49	0.49	0.49	0.49	0.49	0.49	0.49	0.00	0.00	-0.01	0.90
Cl	0.61	0.61	0.61	0.61	0.61	0.61	0.61	0.61	0.61	0.61	0.61	0.61	1.35	-0.01
Sum	99.77	99.77	77.47	76.77	64.52	56.47	48.80	48.30	47.70	46.55	45.71	44.96	99.77	99.77
∑(FeO+Fe_2O_3)	19.19	19.19	—	—	—	—	—	—	—	—	—	—	23.14	16.03
∑(SO_3)	5.54	5.54	—	—	—	—	—	—	—	—	—	—	11.01	0.90
Relative to whole sample			22.3	0.7	12.3	8.0	7.6	0.5	0.6	1.2	0.8	0.8	**45.3**	**54.7**
Relative to XRD crystalline			40.8	1.3	22.4	14.6	13.9	0.9	1.1	2.1	1.5	1.4	—	100.0

*Plagioclase, An57; Olivine, Fo62; Augite, En44Fs20Wo36 (Mg/Fe, 2.2 atomic); Pigeonite, En56Fs35Wo8 (Fe/Mg, 1.6 atomic). †APXS chemistry from Gellert *et al.* (*35*). ‡Cr_2O_3 and MnO calculated with the amorphous component. §Total Fe as FeO+Fe_2O_3 because APXS does not distinguish oxidation states. ‖FeO required for Fe^{2+} crystalline phases (olivine, augite, pigeonite, ilmenite, and magnetite). ¶Fe_2O_3 required for Fe^{3+} crystalline phases (hematite and magnetite). #SO_3 required for crystalline SO_3 crystalline phase (anhydrite).

martian air (0.02 kg/m^3), and g is the acceleration due to gravity (3.71 m/s^2). The calculated u_{*c} is 2.6 m/s, which represents the fluid shear velocity to initiate motion. Because grains in creep derive a portion of their momentum from collisions by saltating grains, on Earth once saltation begins, creep can occur down to 0.7 u_{*c} (1.8 m/s as applied to the Rocknest grains), which represents the impact threshold for motion. Given a boundary layer created by winds blowing over the surface, shear velocities can then be related to the wind speeds above the surface by the law of the wall

$$u_z = \frac{u*}{k} \ln\left(\frac{z}{z_0}\right)$$

where u_z is the wind speed at height z above the surface (taken here as 1 m), k is a constant of 0.407, and z_0 is the roughness height where the idealized logarithmic wind profile is predicted to be zero. Roughness height varies by grain size and the height of surface features, such as wind ripples (*7*), and also by the height and intensity of the saltation cloud (*43*). Rocknest conditions are unknown, but z_0 is taken as 0.3 mm, which would be the roughness height with wind ripples 10 mm in height. Estimated wind speeds at 1 m above the surface are ~52 m/s (116 mph) and 36 m/s (80 mph), without and with saltation, respectively. As a result of the lower gravity and reduced atmospheric density on Mars, a greater hysteresis exists than on Earth between the fluid and impact thresholds, and saltation impacts upon grains are more energetic (*18*, *44*, *45*). The combined effects suggest that initial transport of the coarse surface grains probably occurred at lower wind speeds than those calculated. Conversely, reactivation of the sand shadow would require considerably higher wind speeds because of induration of the surface.

Although observations from the Viking Lander 1 suggest that wind speeds of 30 m/s at a height of 1.6 m occurred during its 2-year lifetime (*46*), we do not known how often Mars winds can be capable of transporting 1- to 2-mm grains. The wind estimates above suggest that formation of the Rocknest sand shadow has involved rare strong winds and that reactivation of the sand shadow from its currently indurated state would require even stronger and rarer winds.

Given the possibility of considerable antiquity of the Rocknest sand shadow and similar coarse-grained bedforms on Mars, could their activation correspond to the martian obliquity cycle? At low obliquities, the atmosphere collapses onto the polar caps, but at high obliquity, CO_2 is released to the atmosphere (*47*, *48*). Taken as an end member, atmospheric density may double at high obliquity and thereby enhance aeolian activity (*48*). As a comparison with the above values calculated for the present martian atmosphere, using 0.04 kg/m^3 for atmospheric density, the calculated fluid u_{*c} is 1.9 m/s and the impact u_{*c} is 1.3 m/s, which correspond to wind speeds at the 1-m height of ~37 m/s (83 mph) and 26 m/s (58 mph), respectively. Although considerably lower than values calculated for present conditions, rare strong wind events are still implied.

References and Notes

1. A Mars solar day has a mean period of 24 hours, 39 min, 35 s and is customarily referred to as a "sol" to distinguish it from the roughly 3% shorter day on Earth.
2. A sand shadow is an accumulation of wind-blown sediment deposited in the lower-velocity lee of an obstacle in the path of the wind.
3. R. C. Anderson *et al.*, Collecting samples in Gale Crater, Mars; An overview of the Mars Science Laboratory Sample Acquisition, Sample Processing and Handling System. *Space Sci. Rev.* **170**, 57–75 (2012). doi: 10.1007/s11214-012-9898-9
4. M. S. Anderson *et al.*, In situ cleaning of instruments for the sensitive detection of organics on Mars. *Rev. Sci. Instrum.* **83**, 105109 (2012). doi: 10.1063/1.4757861; pmid: 23126806
5. D. F. Blake *et al.*, Characterization and calibration of the CheMin mineralogical instrument on Mars Science Laboratory. *Space Sci. Rev.* **170**, 341–399 (2012). doi: 10.1007/s11214-012-9905-1
6. P. R. Mahaffy *et al.*, The sample analysis at Mars investigation and instrument suite. *Space Sci. Rev.* **170**, 401–478 (2012). doi: 10.1007/s11214-012-9879-z
7. R. A. Bagnold, *The Physics of Blown Sand and Desert Dunes* (Chapman and Hall, London, 1941).
8. K. S. Edgett *et al.*, Curiosity's Mars Hand Lens Imager (MAHLI) Investigation. *Space Sci. Rev.* **170**, 259–317 (2012). doi: 10.1007/s11214-012-9910-4
9. W. Goetz *et al.*, Microscopic analysis of soils at the Phoenix landing site, Mars: Classification of soil particles and description of their optical and magnetic properties. *J. Geophys. Res.* **115**, E00E22 (2010). doi: 10.1029/2009JE003437
10. K. E. Herkenhoff *et al.*, In situ observations of the physical properties of the martian surface, in *The Martian Surface: Composition, Mineralogy, and Physical Properties*, J. F. Bell III, Ed. (Cambridge Univ. Press, Cambridge, 2008), pp. 451–467.
11. R. Sullivan *et al.*, Wind-driven particle mobility on Mars: Insights from Mars Exploration Rover observations at "El Dorado" and surroundings at Gusev Crater. *J. Geophys. Res.* **113**, E06S07 (2008). doi: 10.1029/2008JE003101
12. L. A. Soderblom *et al.*, Soils of Eagle Crater and Meridiani Planum at the Opportunity rover landing site. *Science* **306**, 1723–1726 (2004). doi: 10.1126/science.1105127; pmid: 15576606
13. R. Sullivan *et al.*, Aeolian processes at the Mars exploration rover Meridiani Planum landing site. *Nature* **436**, 58–61 (2005). doi: 10.1038/nature03641; pmid: 16001061
14. S. G. Fryberger, P. Hesp, K. Hastings, Aeolian granule ripple deposits, Namibia. *Sedimentology* **39**, 319–331 (1992). doi: 10.1111/j.1365-3091.1992.tb01041.x
15. D. J. Jerolmack, D. Mohrig, J. P. Grotzinger, D. A. Fike, W. A. Watters, Spatial grain size sorting in eolian ripples and estimation of wind conditions on planetary surfaces: Application to Meridiani Planum, Mars. *J. Geophys. Res.* **111**, E12S02 (2006). doi: 10.1029/2005JE002544
16. J. M. Ellwood, P. D. Evans, I. G. Wilson, Small scale aeolian bedforms. *J. Sed. Petrol.* **45**, 554–561 (1975).
17. P. A. Hesp, The formation of shadow dunes. *J. Sed. Petrol* **51**, 101–112 (1981).
18. M. P. Almeida, E. J. R. Parteli, J. S. Andrade Jr., H. J. Herrmann, Giant saltation on Mars. *Proc. Natl. Acad. Sci. U.S.A.* **105**, 6222–6226 (2008). doi: 10.1073/pnas.0800202105; pmid: 18443302
19. M. P. Golombek *et al.*, Constraints on ripple migration at Meridiani Planum from Opportunity and HiRISE observations of fresh craters. *J. Geophys. Res.* **115**, E00F08 (2010). doi: 10.1029/2010JE003628
20. D. L. Bish *et al.*, X-Ray diffraction results from Mars Science Laboratory: Mineralogy of Rocknest at Gale Crater. *Science* **341**, 1238932 (2013); doi: 10.1126/science.1238932
21. Supplementary materials are available on *Science* Online.
22. Unit cell parameters obtained from the RRUFF Project database, http://rruff.info/ima.
23. S. R. Taylor, S. M. McLennan, *Planetary Crusts: Their Composition, Origin and Evolution* (Cambridge Univ. Press, Cambridge, (2009).
24. R. V. Morris *et al.*, Iron mineralogy and aqueous alteration from Husband Hill through Home Plate at Gusev Crater, Mars: Results from the Mössbauer instrument on the Spirit Mars Exploration Rover. *J. Geophys. Res.* **113**, E12S42 (2008). doi: 10.1029/2008JE003201
25. D. W. Ming *et al.*, Geochemical properties of rocks and soils in Gusev Crater, Mars: Results of the Alpha Particle X-ray Spectrometer from Cumberland Ridge to Home Plate. *J. Geophys. Res.* **113**, E12S39 (2008). doi: 10.1029/2008JE003195
26. R. V. Morris *et al.*, Mössbauer mineralogy of rock, soil, and dust at Gusev Crater, Mars: Spirit's journey through weakly altered olivine basalt on the Plains and pervasively altered basalt in the Columbia Hills. *J. Geophys. Res.* **111**, E02S13 (2006). doi: 10.1029/2005JE002584
27. A. S. Yen *et al.*, An integrated view of the chemistry and mineralogy of martian soils. *Nature* **436**, 49–54 (2005). doi: 10.1038/nature03637; pmid: 16001059
28. A. S. Yen *et al.*, Evidence for a global martian soil composition extends to Gale Crater. *45th Lunar and Planetary Science Conference*, March 2013, Published on CD by the Lunar and Planetary Institute, Houston, Texas, Abstract 2495 (2013).
29. J. A. Berger *et al.*, MSL Titanium Observation Tray Measurements with APXS. *45th Lunar and Planetary Science Conference*, March 2013, Published on CD by the Lunar and Planetary Institute, Houston, Texas, Abstract 1321 (2013).
30. R. Gellert *et al.*, Alpha Particle X-ray Spectrometer (APXS): Results from Gusev Crater and calibration report. *J. Geophys. Res.* **111**, E02S05 (2006). doi: 10.1029/2005JE002555
31. Because APXS does not discriminate among iron oxidation states, the total Fe concentration was proportioned in accordance with the oxidation state information carried by the crystalline phases (Table 3, column 3). FeO-Cryst and Fe_2O_3-Cryst are the concentrations of FeO and Fe_2O_3 required to accommodate olivine, augite, pigeonite, ilmenite, and magnetite and hematite, in accordance with their valence states. The remaining iron (FeO + Fe_2O_3) is then associated with the amorphous component without implications for oxidation state. Similarly, some SO_3 is reported as SO_3-Cryst to accommodate anhydrite as a crystalline component.
32. L. A. Leshin *et al.*, Volatile, isotope, and organic analysis of martian fines with the Mars Curiosity Rover. *Science* **341**, 1238937 (2013); doi: 10.1126/science.1238937
33. Nanophase ferric oxide (npOx) is a generic name for amorphous, poorly crystalline, or short-range ordered products of oxidative alteration/weathering that have octahedrally coordinated Fe^{3+} (Mössbauer doublet) and are predominantly oxide/oxyhydroxide/hydrous in nature. Depending on local conditions, npOx (as encountered on Earth) can be any combination of superparamagnetic hematite and goethite, lepidocrocite, ferrihydrite, schwertmannite, akaganeite, hisingerite, and the octahedral Fe^{3+}-rich particles that pigment iddingsite and palagonite. npOx can also incorporate anions like $(SO_4)^{2-}$, Cl^-, and $(PO_4)^{3-}$ through specific chemical adsorption. Because of different local conditions on Mars, one or more forms of npOx on the planet may be uncommon or not present on Earth.
34. P.-Y. Meslin *et al.*, Soil diversity and hydration as observed by ChemCam at Gale Crater, Mars. *Science* **341**, 1238670 (2013); doi: 10.1126/science.1238670
35. R. Gellert *et al.*, Initial MSL APXS activities and observations at Gale Crater, Mars, *45th Lunar and Planetary Science Conference*, March 2013, Published on CD by the Lunar and Planetary Institute, Houston, Texas, Abstract 1432 (2013).

36. H. Y. McSween Jr., G. J. Taylor, M. B. Wyatt, Elemental composition of the martian crust. *Science* **324**, 736–739 (2009). doi: 10.1126/science.1165871; pmid: 19423810
37. S. R. Taylor, S. M. McLennan, *Planetary Crusts: Their Composition, Origin and Evolution* (Cambridge Univ. Press, Cambridge, 2009).
38. R. V. Morris *et al*., Mössbauer mineralogy of rock, soil, and dust at Meridiani Planum, Mars: Opportunity's journey across sulgate-rich outcrop, basaltic sand and dust, and hematite lag deposits. *J. Geophys. Res.* **111**, E12S15 (2006). doi: 10.1029/2005JE002584
39. R. E. Milliken, J. P. Grotzinger, B. J. Thomson, Paleoclimate of Mars as captured by the stratigraphic record in Gale Crater. *GRL* **37**, L04201 (2010). doi: 10.1029/2009GL041870
40. D. H. Lindsley, Pyroxene thermometry. *Am. Mineral.* **68**, 477–493 (1983).
41. P. H. Warren, J. T. Wasson, The compositional-petrographic search for pristine nonmare rocks: Third foray. *Proc. Lunar Planet. Sci. Conf. 10th* (1979), 583–610.
42. Y. Shao, H. Lu, A simple expression for wind erosion threshold friction velocity. *J. Geophys. Res.* **105**, (D17), 22,437–22,443 (2000). doi: 10.1029/2000JD900304
43. P. R. Owen, Saltation of uniform grains in air. *J. Fluid Mech.* **20**, 225–242 (1964). doi: 10.1017/S0022112064001173
44. P. Claudin, B. Andreotti, A scaling law for aeolian dunes on Mars, Venus, Earth, and for subaqueous ripples. *Earth Planet. Sci. Lett.* **252**, 30–44 (2006). doi: 10.1016/j.epsl.2006.09.004
45. J. F. Kok, Difference in the wind speeds required for initiation versus continuation of sand transport on Mars: Implications for dunes and dust storms. *Phys. Rev. Lett.* **104**, 074502 (2010). doi: 10.1103/PhysRevLett.104.074502; pmid: 20366891
46. R. E. Arvidson, E. A. Guinness, H. J. Moore, J. Tillman, S. D. Wall, Three Mars years: Viking Lander 1 imaging observations. *Science* **222**, 463–468 (1983). doi: 10.1126/science.222.4623.463; pmid: 17746178
47. C. E. Newman, S. R. Lewis, P. L. Read, The atmospheric circulation and dust activity in different orbital epochs on Mars. *Icarus* **174**, 135–160 (2005). doi: 10.1016/j.icarus.2004.10.023
48. R. J. Phillips *et al*., Massive CO_2 ice deposits sequestered in the south polar layered deposits of Mars. *Science* **332**, 838–841 (2011). doi: 10.1126/science.1203091; pmid: 21512003

Acknowledgments: Support from the NASA Mars Science Laboratory Mission is gratefully acknowledged. The chemical and mineralogical data presented here are derived from the archived data sets in the NASA Planetary Data System (PDS) http://pds-geosciences.wustl.edu/missions/msl, specifically MSL-M-CHEMIN-2-EDR-V1.0 and MSL-M-APXS-2-EDR-V1.0. M.B.M. was funded by the Danish Council for Independent Research/Natural Sciences (Det Frie Forskningsråd Natur og Univers FNU grants 12-127126 and 11-107019). W.G. acknowledges partial funding by the Deutsche Forschungsgemeinschaft (DFG grant GO 2288/1-1). Some of this research was carried out at the Jet Propulsion Laboratory, California Institute of Technology, under a contract with NASA.

Supplementary Materials

www.sciencemag.org/content/341/6153/1239505/suppl/DC1
Supplementary Text
Figs. S1 to S4
Tables S1 and S2
References

23 April 2013; accepted 31 July 2013
10.1126/science.1239505